**PAPER**

# Al$_2$O$_3$(11$\bar{2}$0) surface as a template for the ordered growth of Ni and Co nanoclusters

**Krithika Venkataramani,**[a] **Thomas N. Jensen,**[a] **Stig Helveg,**[b] **Michael Reichling,**[c] **Flemming Besenbacher**[a] **and Jeppe V. Lauritsen\***[a]

The morphology and thermal stability of Ni and Co nanoclusters grown by physical vapour deposition on a reconstructed (11$\bar{2}$0) surface of α-Al$_2$O$_3$ is investigated using non-contact atomic force microscopy (NC-AFM). NC-AFM images reveal that the clean α-Al$_2$O$_3$(11$\bar{2}$0) substrate adopts a characteristic (12 × 4) reconstruction when prepared in vacuum at high temperature. Subsequent deposition of Ni and Co onto this substrate at room temperature facilitates the growth of well-ordered metal nanocluster arrays with a preferred inter-cluster distance determined by the (12 × 4) periodicity of the substrate surface. The order in the cluster arrangement remains intact even upon annealing the system to temperatures up to 500 °C indicating a high resistance against sintering. The reconstructed α-Al$_2$O$_3$(11$\bar{2}$0) surface can, therefore, serve as an appropriate insulating template for studies of size-dependent magnetic or catalytic effects in a well-defined ensemble of metallic nanoclusters.

## Introduction

Alumina is a technologically very important material used as substrates for thin films, for structural ceramics, as corrosion barriers or high thermal-conductivity dielectric supports.[1] Alumina in various porous forms[2] is also extensively used either as a catalyst or as a support for catalytically active nanoparticles in a wide range of catalysts.[3] Understanding the basic properties of clean and hydrated alumina surfaces and their interactions with metals has, therefore, been a topic of extensive research over many years. However, a detailed description of such phenomena on Al$_2$O$_3$ surfaces is still severely hampered by a lack of the atomic-scale understanding of the surface structure of Al$_2$O$_3$. Some progress has been made in terms of structural studies of the most stable (0001) surface of α-Al$_2$O$_3$ (sapphire),[1,4–13] however, the insulating nature of this oxide surface remains an obstacle for applying the full range of electron and ion-based surface science techniques. By theoretical modelling one could gain new insight into several fundamental phenomena on alumina surfaces such as adsorption, hydration and hydroxylation effects,[14–20] adhesion of metals[21–27] and surface diffusion and sintering,[28–30] all of which are of importance for understanding the industrial use of alumina. However, due to the above-mentioned difficulties in characterisation and as single-crystal alumina surfaces are generally difficult to prepare and to handle, a sufficient level of experimental insight has not been achieved. Dynamic scanning force microscopy (SFM) operated in the so-called non-contact mode (NC-AFM) has over the last few years been established as a standard tool for highest resolution imaging of oxide surfaces[31,32] and has not only provided atomic-scale images of α-Al$_2$O$_3$(0001)[33–35] and alumina thin films,[36,37] but also morphological characterization of nanoclusters supported on alumina surfaces.[38–40] Compared to the α-Al$_2$O$_3$(0001) surface (often referred to as the *c*-face), much less systematic studies are available for the high temperature phases of the α-Al$_2$O$_3$(11$\bar{2}$0) (*a*-face) of α-Al$_2$O$_3$.[41,42–48] Due to the broken symmetry of the (11$\bar{2}$0) surface, the surface is expected to contain terminal O and Al atoms in a different coordination compared to the (0001) surface what is anticipated to yield specific properties in terms of surface hydroxylation[48] and for metal adhesion.[49–52] Since the *a* and *c*-faces of α-Al$_2$O$_3$ are perpendicular to each other, they possess distinct symmetries and, furthermore, have different surface energies[53] what may be exploited to produce uniform nanoscale alumina structures.[54,55]

Here we use NC-AFM to study the structure of the α-Al$_2$O$_3$(11$\bar{2}$0) surface prepared at high temperature under UHV conditions and analyse the morphology, growth and thermal stability of Ni and Co nanoclusters on this surface. Plain α-Al$_2$O$_3$(11$\bar{2}$0) is found to be (12 × 4) reconstructed. We find that Ni and Co deposited by physical vapour deposition on this surface grow in the form of uniformly sized nanoclusters

*$^a$ Interdisciplinary Nanoscience Center (iNANO), University of Aarhus, Ny Munkegade 118, DK-8000 Aarhus C, Denmark. E-mail: jvang@inano.au.dk; Fax: +45 8942 3690; Tel: +45 8942 5537*
*$^b$ Haldor Topsøe A/S, Nymøllevej 55, DK-2800 Kgs. Lyngby, Denmark*
*$^c$ Fachbereich Physik, Universität Osnabrück, Barbarastraße 7, 49076 Osnabrück, Germany*

2092 | *Phys. Chem. Chem. Phys.*, 2012, **14**, 2092–2098

This journal is © the Owner Societies 2012

which are periodically placed at positions reflected by the periodicity of the (12 × 4) reconstructed substrate. The average height and width of the clusters are for both systems estimated by means of NC-AFM measurements, and although a systematic study for different coverages is not reported here, the results show that ordering is kept at a coverage up to 0.3 ML. Interestingly, the ordering associated with the template effect is also surprisingly robust against thermal treatment, in particular in the 12-fold direction, since the alignment of nanoclusters on the surface in rows is evident even after heating to temperature in excess of 600 °C. The observations furthermore suggest that mass transport on the surface is highly unidirectional along the reconstruction-induced stripes. Therefore, this system may be an attractive model system for quantitative microscopic studies of mass transport and sintering of very small metal nanoclusters.[56,57]

## Materials and methods

The experimental setup consists of an ultra-high vacuum (UHV) chamber with a base pressure of $\sim 1 \times 10^{-10}$ mbar. The chamber is equipped with a variable temperature atomic force microscope (VT-AFM, Omicron Nanotechnology GmbH, Taunusstein, Germany) with an Easy PLLplus control unit (Nanosurf AG, Liestal, Switzerland) for improved excitation of the cantilever oscillation and frequency shift detection. All experiments are performed by operating the AFM in the dynamic, non-contact mode using commercial uncoated cantilevers (Super Sharp Silicon-NCH type, Nanosensors, Neuchâtel, Switzerland) with a spring constant of about 19 N m$^{-1}$ and resonance frequencies in the range of 280 to 320 kHz. The peak-to-peak amplitude of the cantilever oscillation is stabilized to about 20 nm. For this study, all new tips are cleaned by gentle Ar$^+$ bombardment (2 keV, 5–15 s). NC-AFM images are recorded in the *topography mode*, i.e. by keeping the mean frequency shift due to the tip–surface interaction constant relative to a pre-set frequency shift ($\Delta f$) value and recording the feedback signal of the tip–surface distance control.[58] The voltage applied to the tip relative to the sample holder, $U_{\text{bias}}$, is adjusted regularly to minimise the electrostatic forces arising from the contact potential difference. NC-AFM image analysis is performed with a scanning probe image processor (SPIP, Image Metrology A/S, Hørsholm, Denmark).
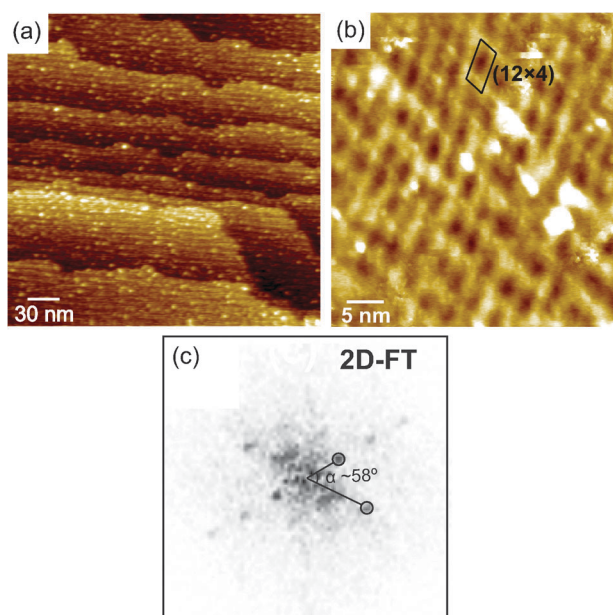
AFM studies are performed on a freshly prepared surface of a single crystal of α-Al$_2$O$_3$(11$\bar{2}$0) of dimensions 10 mm × 2 mm × 0.5 mm (MTI Corporation, Richmond CA, USA). Prior to mounting the crystal in the UHV system, the sample is cleaned *ex situ* in 35% HNO$_3$ for 30 min, rinsed in water and then annealed in a tube furnace for 8 h at 1200 °C under atmospheric conditions. For sample preparation in UHV, the crystal undergoes several cycles of Ar$^+$ bombardment (1.5 keV, 15 min) and subsequent annealing up to 1200 °C. The sample temperature is monitored contact-less on the face of the crystal using an optical pyrometer (Metis MY81, Sensortherm GmbH, Sulzbach, Germany) that has been calibrated against a K-type thermocouple in direct contact with the sample. Prior to each deposition experiment, the sample is subjected to one additional cleaning cycle. We monitor the surface cleanliness both before and after metal deposition by X-ray photoelectron spectroscopy (XPS) using Mg K$_\alpha$

radiation (Phoibos 100 analyser and XR 50 X-ray source, SPECS GmbH, Berlin, Germany). XPS spectra are recorded with the surface normal pointing in the direction of the analyser. Fig. 1a shows the XPS spectrum of a clean α-Al$_2$O$_3$(11$\bar{2}$0) surface prepared by the procedure described above. The surface is found to be free from carbon contamination below the $\sim 0.02$ ML detection limit of the system as evidenced by the absence of the C(1s) peak at a binding energy of $\sim 284$ eV. No other peaks attributed to impurities could be detected in the XPS scans, but nevertheless the NC-AFM images always revealed a small amount of impurity patches on the surface (Fig. 2b). The very low coverage and height of the impurity patches are, however, not seen to influence the measurements of the average dimension of the deposited nanoclusters.

Metallic Ni and Co are deposited by physical vapour deposition onto the substrate at room temperature by means
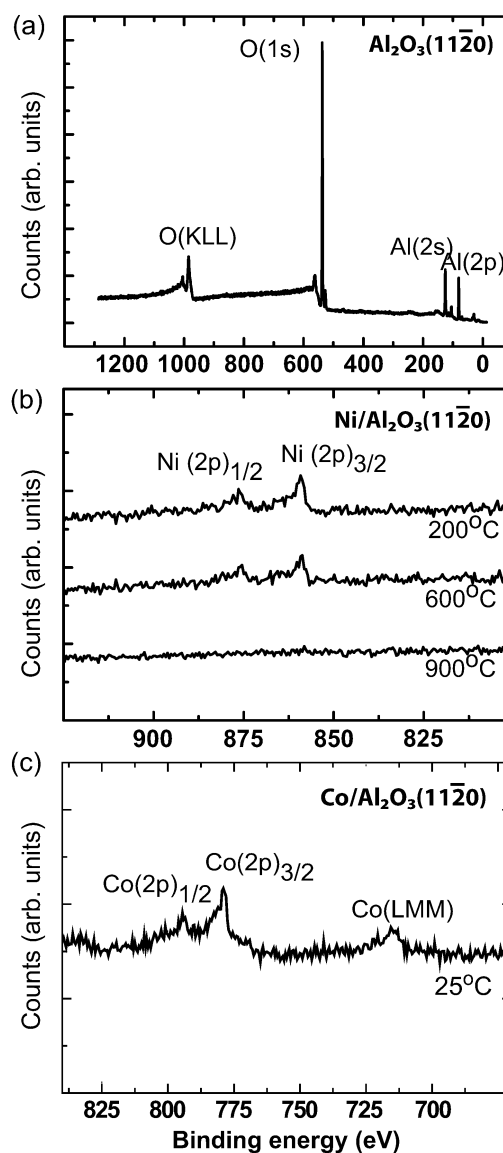


**Fig. 1** (a) XPS survey scan of the clean α-Al$_2$O$_3$(11$\bar{2}$0) surface after preparation. (b) XPS spectra showing the Ni(2p) signals after 0.15 ML Ni deposition and subsequent annealing at 200 °C, 600 °C and 900 °C, respectively. (c) XPS spectrum of the surface exposed to 0.3 ML Co.

This journal is © the Owner Societies 2012

*Phys. Chem. Chem. Phys.*, 2012, **14**, 2092–2098 | 2093

**Fig. 2** (a) Large scale image of the surface topography of α-Al₂O₃(11̄20) after several sputter/anneal cycles involving heating to 1200 °C in UHV. (b) High resolution NC-AFM image of the (12 × 4) reconstruction (constant frequency shift $\Delta f = -35$ Hz, $U_{bias} = -1.24$ V). The white patches on the surface reflect a surface impurity of unknown origin. (c) 2D Fourier transform power spectrum of the image from (b) with circles highlighting the main reflections and facilitating a precise analysis of the (12 × 4) reconstruction.

of a water-cooled e-beam evaporator (EGN4, Oxford Applied Research, Witney, United Kingdom) from 2 mm Ni and Co rods (99.99% purity, Goodfellow, Huntingdon, United Kingdom), respectively. The flux is adjusted to yield a deposition rate of $\sim 0.15$ ML min⁻¹ for Ni and $\sim 0.3$ ML min⁻¹ for Co. Prior to metal deposition, the source is thoroughly outgassed for several hours and the base pressure of the chamber during deposition never exceeds $6 \times 10^{-10}$ mbar. To avoid damage and charging of the surface, it is important to prevent ions, generated during the electron bombardment of the metal rods, from reaching the surface. To reduce the influence of charges, a positively biased metal grid in the top piece of the evaporator acts as an ion-repeller by deflecting ionized metal atoms. Residual surface charge is eliminated by exposing the metal deposited surface to a short pulse (7–9 s, 0.2 mA emission) from an electron flood gun providing electrons of 2 eV energy. The forces due to remaining surface charges that cannot be eliminated in the described way are minimized before AFM imaging by applying a bias on the AFM tip relative to the sample support as described in ref. 59.

Fig. 1b shows an XPS spectrum of the Ni deposited surface in the Ni(2p) energy region. The Ni $(2p)_{1/2}$ and $(2p)_{3/2}$ peaks are both observed as rather broad features at binding energies of $\sim 877$ eV and $\sim 860$ eV, respectively, with the expected intensity ratio of 2 : 3. The binding energy values are neither directly compatible with values for metallic Ni(0) (Ni$(2p)_{3/2}$ at 852.7 eV) nor with values for oxidized species (Ni$(2p)_{3/2}$ at 854–856 eV).[60] We attribute the observed peak shift and broadening of the peak to surface charging during photoemission.

In principle, a comparison of the shift of the Al and O peaks in the spectrum allows one to extract the peak position, but the width itself of the peak excludes a firm conclusion regarding the chemical shift. Similarly, the XPS spectrum of the Co deposited surface is shown in Fig. 1c, where the Co $(2p)_{3/2}$ peak is observed at $\sim 779$ eV. The corresponding databook values for the Co$(2p)_{3/2}$ peak position is 779.9 eV for metallic Co(0) and 779.4–780.7 eV for oxidized Co.[60]

## Results and discussion

### Surface structure of clean α-Al₂O₃(11̄20)

Fig. 2a shows a large scale topographic image of the freshly prepared α-Al₂O₃(11̄20) surface. After the first few annealing cycles of a fresh sample, the formation of terraces is observed but the surface is still comparatively rough as has been observed previously.[61–63] Further annealing cycles result in a fairly flat surface with large terraces bound by step edges aligned in the [1̄100] direction in Fig. 2a. The step height is about 0.24 nm or multiples of this value. This corresponds to single or multiple atomic steps, where a single atomic step height is defined as the distance between two subsequent Al planes in the bulk alumina structure which is 0.238 nm.[41,63] Fig. 2a, furthermore, reveals an atomic scale row structure decorating the terraces where the rows are aligned parallel to the step edges. This structure points to the formation of a large unit cell reconstruction. Surface reconstruction is well known for the case of Al₂O₃(0001), where annealing at step-wise increased temperature invokes a series of rotational reconstructions[9,13] until the most stable $\sqrt{31} \times \sqrt{31}$ R9° high temperature reconstruction is reached.[33–35] For the α-Al₂O₃(11̄20) surface, reconstruction results in the formation of a rhombic unit cell related to the grid of bright lines as evident from the high-resolution image shown in Fig. 2b. The 2-dimensional Fourier transform power spectrum shown in Fig. 2c is used to determine the atomic distances and the orientation of the two high-symmetry directions of the super-structure. We find two clearly distinct peaks reflecting a 3.3 nm periodicity in one direction, a 6.2 nm periodicity in the other direction and an angle of 58° enclosed by the reconstructed surface unit cell vectors. As evident from the comparison of
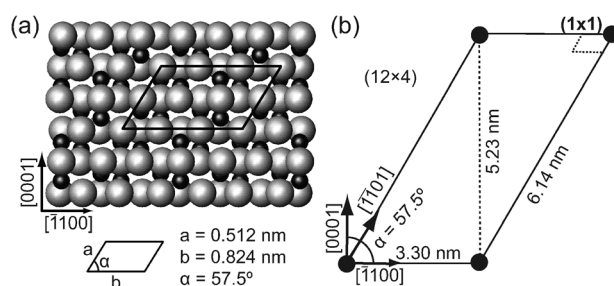


**Fig. 3** (a) Top view ball model of the O-terminated (1 × 1)-Al₂O₃(11̄20) surface obtained from a bulk truncation. Large grey spheres denote O atoms while small black spheres denote Al atoms. The surface unit cell is outlined by the black rhombus with dimensions a and b, respectively. (b) Unit cell dimensions of the (12 × 4) reconstructed Al₂O₃(11̄20) surface. For comparison, the (1 × 1)-Al₂O₃(11̄20) unit cell is indicated by the dashed rhombus.

unit cells drawn to scale in Fig. 3a and b, the unit cell of the reconstructed surface is much larger than the unit cell of bulk-truncated α-Al$_2$O$_3$(11$\bar{2}$0).[41,47] The reconstructed surface unit cell corresponds to a (12 × 4) reconstruction, a finding that is in agreement with models derived from results of previous LEED, He-scattering and contact mode AFM studies.[41,42,45]

Becker et al.[41] proposed that the (12 × 4) reconstruction is due to the reduction of O on the surface by ∼50% compared to the (1 × 1) structure leading to the formation of a regular arrangement of oxygen vacancies on the surface. Recently, based on X-ray reflectivity data[48] it has been proposed, however, that surface reconstruction is a consequence of the removal of Al–O complexes. The corrugation measured in NC-AFM line scans along the high symmetry directions is 0.1 to 0.2 nm, which is in general comparable with the geometric feature expected from such vacancy formation. However, no internal structure is visible inside the rhombic unit cells in the NC-AFM image in Fig. 2c and further high-resolution NC-AFM studies are needed to settle the details of the atomic structure of the (12 × 4) reconstructed surface.

### Ni and Co deposition on the reconstructed α-Al$_2$O$_3$(11$\bar{2}$0) surface

Fig. 4a and 5a show NC-AFM images of the (12 × 4) reconstructed α-Al$_2$O$_3$(11$\bar{2}$0) surface with an estimated coverage of 0.15 ML Ni and 0.3 ML Co, respectively, after flash annealing the surface at 200 °C. From these images, it is evident that both Ni and Co nucleate in rows with a periodic structure along the [$\bar{1}$100] direction. As illustrated by the line scans in Fig. 4c for Ni and Fig. 5c for Co, the periodicity perpendicular to the rows is found to be 5.2 nm (illustrated with grid lines). This distance coincides well with the diagonal
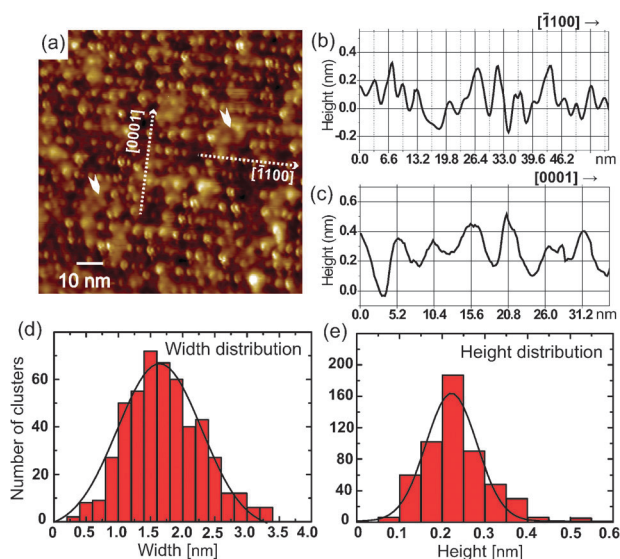


**Fig. 4** (a) NC-AFM image of the Ni exposed, reconstructed Al$_2$O$_3$(11$\bar{2}$0) surface (0.15 ML) after annealing at 200 °C for 3 min (constant frequency shift Δf = −26.0 Hz, V$_{bias}$ = 7.0 V). (b) Line scan (average of 7) along a row of nanoclusters. The grid lines reflect the expected 3.3 nm periodicity. (c) Line scan (average of 5) in the direction perpendicular to the rows. The grid lines reflect the expected 5.2 nm periodicity. (d) Particle width distribution (PWD) and (e) particle height distribution (PHD) for the Ni nanoclusters on Al$_2$O$_3$(11$\bar{2}$0).
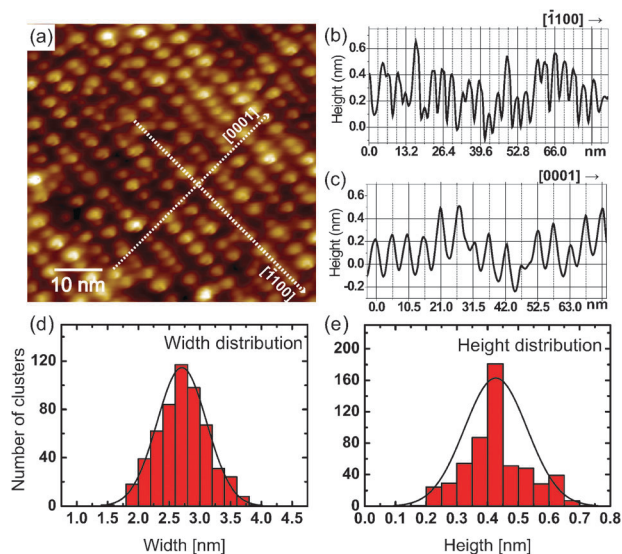


**Fig. 5** (a) NC-AFM image of 0.3 ML Co deposited on the reconstructed Al$_2$O$_3$(11$\bar{2}$0) surface after annealing to 200 °C for 3 min (constant frequency shift Δf = −22.0 Hz, V$_{bias}$ = 6.4 V). (b) Line scan (average of 5) along a row of Co nanoclusters. The grid lines reflect the expected 3.3 nm periodicity. (c) Line scan (average of 5) in the direction perpendicular to the nanocluster rows. The grid lines reflect the expected 5.2 nm periodicity in this direction. (d) Particle width distribution (PWD) and (e) particle height distribution (PHD) for the Co nanoclusters on Al$_2$O$_3$(11$\bar{2}$0).

length of the (12 × 4) unit cell shown in the model in Fig. 3b. The periodicity along [$\bar{1}$100] shown in line scans in Fig. 4b and 5b is found to be 3.3 nm matching the 4-fold side length of the (12 × 4) unit cell. The nucleation and growth of Ni and Co nanoclusters into a regular structure is thus clearly guided by the (12 × 4) reconstruction. The formation of periodic super-structures by large surface reconstructions or by lattice mismatch in thin films is a common phenomenon observed for thin film oxide overlayers on metallic substrates[36,64–66] and in the case of the growth of one metal onto another with different lattice constants.[67] Such substrate structures have often been used as templates for the growth of uniform well-ordered nanoscale arrays of metal nanoclusters.[68–72] In a recent study of the Al$_2$O$_3$(0001) a-face, it has been demonstrated that the high temperature $\sqrt{31} \times \sqrt{31}$R9° reconstructed surface of Al$_2$O$_3$(0001) can act as a nanotemplate for the controlled growth of almost monodisperse Ni nanoclusters, which was explained by a preference for Ni to nucleate and grow on a certain site within the reconstruction unit cell.[38] In the present work we thus show that also the α-Al$_2$O$_3$(11$\bar{2}$0) surface may act as a template for the growth of well-defined metal clusters, exemplified here for Ni and Co nanostructures.

It should be noted that the long-range regularity along the [$\bar{1}$100] direction with the 4-fold periodicity is not as pronounced as the regularity in the direction perpendicular to the rows. This is attributed to irregularities or impurities present on the initially prepared substrate, which could also sometimes be observed directly in the NC-AFM of the clean surface. NC-AFM images taken at a reduced cluster density compared to the starting situation (see Fig. 6d and e discussed in the next section) reveal that the Ni nanoclusters are preferentially
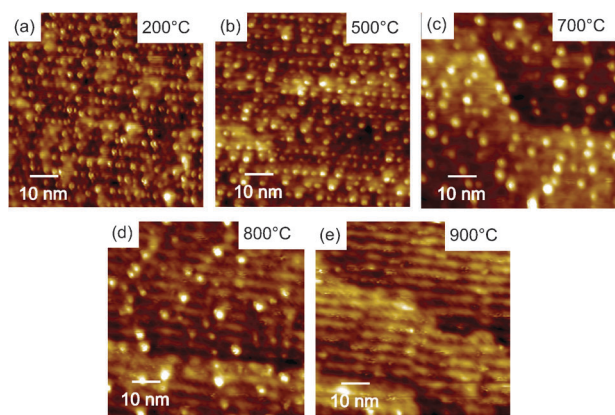
**Fig. 6** A temperature series of NC-AFM images showing the evolution of the Ni nanoclusters after subsequent annealing at temperatures in the range of 200 °C to 900 °C (3 min annealing time at each temperature).

located directly on the bright stripes indicating that the adhesion of Ni is stronger there than that in the darker areas defined by the (12 × 4) reconstruction.

The particle width distribution (PWD) and particle height distribution (PHD) of the Ni and Co nanoclusters are derived from line profiles taken for a large number of nanoclusters in NC-AFM images. The resulting distributions are illustrated in the form of histograms in Fig. 4d and e for Ni nanoclusters and Fig. 5d and e for Co nanoclusters, respectively. An estimate of the width of the nanoclusters is obtained as the full width at half maximum (FWHM) of the profile and the height is measured as the distance from the top facet of the cluster to the substrate surface level beneath. It should be noted that tip convolution effects can influence the apparent size of the nanoclusters if that is comparable to the nominal radius of the tip ($\sim 2.0$ nm for the tips used here). In this study, the values reported for the width of the nanoclusters are not corrected for tip convolution effects since the precise nano-tip shape and its size are unknown. Rather, the true width of the Ni nanoclusters is anticipated to be somewhat smaller than that reported here. By fitting the PWD histogram in Fig. 4d to a Gaussian function, the mean width of the Ni nanoclusters is estimated to be $1.6 \pm 0.3$ nm, reflecting a narrow range of cluster sizes. The mean of the height distribution of the Ni nanoclusters is found to be 0.22 nm closely resembling the distance of 0.203 nm between Ni(111) planes in fcc Ni. A small fraction ($<3\%$) of the registered clusters in the PHD histogram (Fig. 4e) have a height of more than 0.4 nm, reflecting that two-layer islands are present too. However, the majority of the Ni nanoclusters clearly adopt a single atomic layer height. Correspondingly for the Co nanoclusters with results for a slightly higher 0.3 ML coverage shown in Fig. 5d, a width of $2.7 \pm 0.4$ nm is deduced from the PWD. Due to the higher amount of deposited Co, the formation of two-layer Co nanoclusters, corresponding to a height of 0.4 nm, is found to be predominant in the PHD histogram in Fig. 5e, where the distance between the close-packed planes in hcp or fcc stacked Co is 0.204 nm. Again, a small fraction ($<8\%$) of the registered clusters in the PHD histogram for Co (Fig. 5e) have a height of more than 0.6 nm, reflecting that three-layer islands are present for Co.

## Thermal stability of Ni nanoclusters on $\alpha$-Al$_2$O$_3$(11$\bar{2}$0)

To study the effect of thermally induced mass transport and resulting changes in cluster size and morphology, we record a series of NC-AFM images of the Ni nanoclusters after successive annealing for 3 min at five temperatures ranging from 200 °C to 900 °C. Respective NC-AFM images have been taken after cooling the sample down to room temperature and are shown in Fig. 6a–e. The evolution of particle coarsening as a function of annealing temperature is analysed by determining the mean particle height (Fig. 7a) and the mean particle width (Fig. 7b) from individual PWD and PHD histograms and the cluster density (Fig. 7c).

Images shown in Fig. 6a and b do not exhibit any significant change regarding Ni cluster size and dispersion and the (12 × 4) lattice is basically retained in the temperature interval from 200 °C to 500 °C. This shows that the nanometre sized particles are quite robust against sintering on the reconstructed
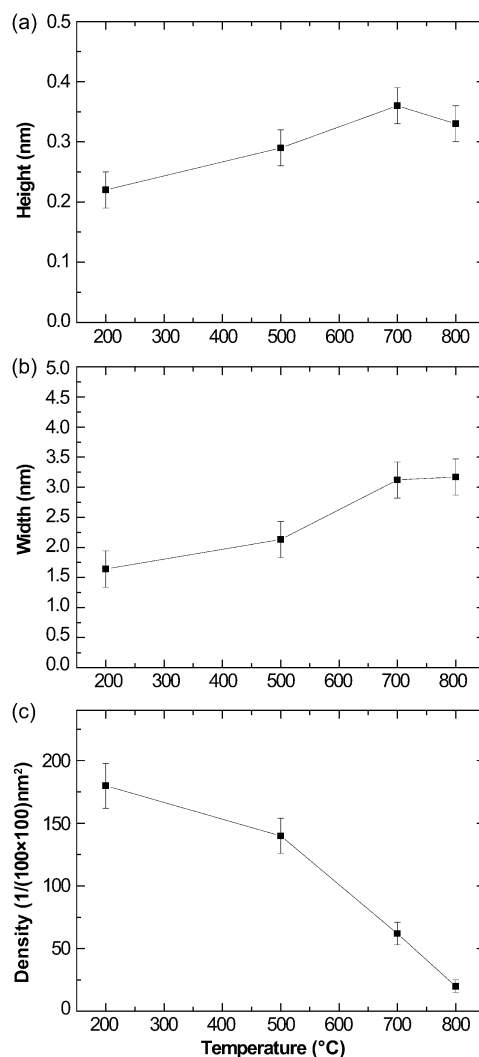


**Fig. 7** (a) Size and density analysis of Ni nanoclusters on $\alpha$-Al$_2$O$_3$(11$\bar{2}$0) obtained from NC-AFM data as a function of the annealing temperature. (a) Mean value and statistical variation (error bar) of the height of the Ni clusters determined from a PHD for each $T$. (b) Mean value and statistical variation (error bar) of the width of the Ni clusters. (c) Number density of Ni nanoclusters per 100 × 100 nm$^2$.

$\alpha\text{-Al}_2\text{O}_3(11\bar{2}0)$ surface. The plots in Fig. 7a and d for the cluster height and width reveal a slight increase in the average dimensions of the Ni nanoclusters, which is, however, smaller than the statistical uncertainty. We conclude that clusters are not, or only minimally, affected by thermal treatment in this temperature range. When further increasing the annealing temperature to 700 °C (Fig. 6c), coarsening is observed by a significant shift of height and width distributions towards larger values. The mean of the height distribution increases to a value of $\sim 0.35$ nm reflecting the formation of two-layer nanoclusters (Fig. 7a). The number density of the Ni nanoclusters on the surface reduces to about a third of the value for annealing to 200 °C (Fig. 7c). An inspection of the NC-AFM image for 700 °C annealing temperature shown in Fig. 6c also reveals that coarsening is accompanied by a release of nanoclusters from the regular arrangement along the rows, whereas the confinement perpendicular to the rows is retained. The coarsening of the Ni nanoclusters observed by annealing at 700 °C is a typical result of particle sintering either by Ostwald ripening, in which individual metal atoms leave a metal nanocluster and join another one, or cluster diffusion and coalescence.[56,73–75] Effectively this means that upon annealing, the formation of two-layer Ni nanoclusters is energetically favoured at the expense of single layer clusters. As the confinement perpendicular to the rows is still strong while the inter-cluster distance along the rows are several multiples of the original value, a likely scenario is that diffusion during coarsening is constrained to the dimension along the stripes of the reconstructed surface.

After annealing to 800 °C, the average width (Fig. 7b) continues to increase to a value of 3.1 nm, whereas the average cluster height still reflects two-layer nanoclusters. Obviously, the amount of Ni on the surface drops further (Fig. 7c) indicating that Ni is lost from the surface. An estimate of the Ni coverage from the cluster density and the cluster dimensions based on a spherical cap model of the nanoclusters shape reveals a 61% reduction in the amount of Ni on the surface at 800 °C compared to the situation at 200 °C. This trend continues for annealing to 900 °C, where all Ni nanoclusters disappear (see Fig. 6e). Also in NC-AFM images taken after annealing to 900 °C with a frame size much larger than the one used for obtaining images from Fig. 6, we do not find any clusters, not even at step edges. This result is fully corroborated by corresponding XPS spectra of the Ni exposed surface taken in the Ni(2p) region after annealing at different temperatures as shown in Fig. 1b. By comparing the relative area of the Ni(2p) peaks in the XPS spectra, the Ni signal at 600 °C is calculated from the intensities to be reduced by $\sim 10\%$ as compared to that at 200 °C and finally at 900 °C, no Ni can be detected on the surface with XPS.

It is well known that the Ni may react with the $\text{Al}_2\text{O}_3$ at elevated temperature to form a very stable nickel aluminate $(\text{NiAl}_2\text{O}_4)$ compound with the spinel structure.[76] However, since both XPS and NC-AFM results clearly point to the removal of nickel when annealing to 900 °C, the formation of $\text{NiAl}_2\text{O}_4$ would have to be postulated taking place deep in the crystal, at least beyond the probing depth of XPS which is several nm in our case. Instead, we attribute the strongly decreasing amount of Ni on the surface above 700 °C to the sublimation of Ni atoms into the vacuum. Hence, all Ni is lost before $\text{NiAl}_2\text{O}_4$ could be formed. This is a plausible interpretation despite the melting point of bulk Ni being at 1453 °C as sublimation from nanoclusters may take place at temperatures significantly below the melting temperature. Such size effects are very important for the explanation of the sintering behaviour of nanoclusters,[56] and a particle size effect on the desorption temperature has previously been observed for, e.g., Cu on alumina thin films using temperature-programmed desorption spectroscopy (TPD).[77] We, therefore, consider this effect to be the most likely scenario explaining our experimental findings.

## Summary

Using NC-AFM we have characterized the growth of Ni and Co nanoclusters on the $\alpha\text{-Al}_2\text{O}_3(11\bar{2}0)$ surface. When prepared at 1200 °C, the surface adopts a $(12 \times 4)$ reconstruction appearing in high-resolution NC-AFM images as a grid of bright stripes defined by the 3.3 nm $\times$ 6.1 nm rhombic unit cell. Subsequent deposition of Ni or Co on the clean reconstructed surface at room temperature yields the formation of a regular pattern of nanoclusters reflecting the periodicity of the reconstruction unit cell that effectively acts as a template for the growth of the metal nanoclusters. Detailed NC-AFM characterization reveals that cluster ensembles are highly uniform consisting of 1.6 nm wide single-layer Ni clusters for a 0.15 ML coverage and 2.6 nm wide two-layer Co nanoclusters for a coverage of 0.3 ML. This difference is expected from the difference in the coverage used in these experiments. However, to fully quantify any important differences in the growth and coalescence of Co and Ni on the reconstructed $\alpha\text{-Al}_2\text{O}_3(11\bar{2}0)$ surface, an experimental NC-AFM series comparing several different coverages up to 1 ML should be performed. When annealing the Ni system to temperatures up to 500 °C, the ensemble of nanoclusters is preserved. However, when annealing at higher temperatures, coalescence is observed with the row-like alignment of nanoclusters being preserved. This indicates unidirectional mass transport during sintering. Annealing at higher temperatures results in a loss of Ni from the surface which is attributed to sublimation of metallic Ni from the surface. The confinement of 1 to 3 nm wide Ni and Co nanoclusters on the reconstructed $\alpha\text{-Al}_2\text{O}_3(11\bar{2}0)$ surface is an effect that may be used for future systematic studies of magnetic or catalytic size-effects associated with metallic or oxidic nanoclusters synthesized on an insulating alumina substrate. We also speculate that the strong confinement of clusters in rows may be used for the formation of regular Ni or Co nanowires on reconstructed $\alpha\text{-Al}_2\text{O}_3(11\bar{2}0)$.

## Acknowledgements

This journal is © the Owner Societies 2012

*Phys. Chem. Chem. Phys.*, 2012, **14**, 2092–2098 | 2097

## Notes and references

1  M. Gautier, G. Renaud, L. P. Van, B. Villette, M. Pollak, N. Thromat, F. Jollet and J. P. Duraud, *J. Am. Ceram. Soc.*, 1994, **77**, 323–334.
2  K. Wefers and M. Chanakya, *Oxides and Hydroxides of Aluminum*, Alcoa Laboratories, 1987.
3  H. Knözinger and P. Ratnasamy, *Catal. Rev.: Sci. Eng.*, 1978, **17**, 31–70.
4  C. C. Chang, *J. Appl. Phys.*, 1968, **39**, 5570.
5  T. M. French and G. A. Somorjai, *J. Phys. Chem.*, 1970, **74**, 2489–2496.
6  I. Vilfan, T. Deutsch, F. Lancon and G. Renaud, *Surf. Sci.*, 2002, **505**, L215–L221.
7  G. Renaud, B. Villette, I. Vilfan and A. Bourret, *Phys. Rev. Lett.*, 1994, **73**, 1825–1828.
8  E. A. Soares, M. A. Van Hove, C. F. Walters and K. F. McCarty, *Phys. Rev. B: Condens. Matter*, 2002, **65**, 13.
9  J. Toofan and P. R. Watson, *Surf. Sci.*, 1998, **401**, 162–172.
10  L. Pham Van, J. Cousty and C. Lubin, *Surf. Sci.*, 2004, **549**, 157–164.
11  S. Ahn and J. W. Rabalais, *Surf. Sci.*, 1997, **388**, 121–131.
12  P. J. Eng, T. P. Trainor, G. E. Brown, G. A. Waychunas, M. Newville, S. R. Sutton and M. L. Rivers, *Science*, 2000, **288**, 1029–1033.
13  M. Gautier, J. P. Duraud, L. P. Van and M. J. Guittet, *Surf. Sci.*, 1991, **250**, 71–80.
14  K. C. Hass, W. F. Schneider, A. Curioni and W. Andreoni, *Science*, 1998, **282**, 265–268.
15  K. C. Hass, W. F. Schneider, A. Curioni and W. Andreoni, *J. Phys. Chem. B*, 2000, **104**, 5527–5540.
16  Z. Lodziana, J. K. Nørskov and P. Stoltze, *J. Chem. Phys.*, 2003, **118**, 11179–11188.
17  X.-G. Wang, A. Chaka and M. Scheffler, *Phys. Rev. Lett.*, 2000, **84**, 3650–3653.
18  P. D. Tepesch and A. A. Quong, *Phys. Status Solidi B*, 2000, **217**, 377–387.
19  R. Di Felice and J. E. Northrup, *Phys. Rev. B: Condens. Matter*, 1999, **60**, R16287–R16290.
20  A. Hellman and H. Grönbeck, *Phys. Rev. Lett.*, 2008, **100**, 116801.
21  Z. Lodziana and J. K. Nørskov, *Surf. Sci.*, 2002, **518**, L577–L582.
22  Z. Lodziana and J. K. Nørskov, *J. Chem. Phys.*, 2001, **115**, 11261–11267.
23  E. A. A. Jarvis and E. A. Carter, *J. Phys. Chem. B*, 2001, **105**, 4045–4052.
24  J. F. Sanz and N. C. Hernandez, *Phys. Rev. Lett.*, 2005, **94**, 016104.
25  B. Hinnemann and E. A. Carter, *J. Phys. Chem. C*, 2007, **111**, 7105–7126.
26  C. Verdozzi, D. R. Jennison, P. A. Schultz and M. P. Sears, *Phys. Rev. Lett.*, 1999, **82**, 799–802.
27  E. Wallin, J. M. Andersson, E. P. Munger, V. Chirita and U. Helmersson, *Phys. Rev. B: Condens. Matter*, 2006, **74**, 125409.
28  R. Meyer, Q. F. Ge, J. Lockemeyer, R. Yeates, M. Lemanski, D. Reinalda and M. Neurock, *Surf. Sci.*, 2007, **601**, 134–145.
29  J. Sehested, J. A. P. Gelten, I. N. Remediakis, H. Bengaard and J. K. Nørskov, *J. Catal.*, 2004, **223**, 432–443.
30  J. Sehested, J. A. P. Gelten and S. Helveg, *Appl. Catal., A*, 2006, **309**, 237–246.
31  J. V. Lauritsen and M. Reichling, *J. Phys.: Condens. Matter*, 2010, **22**, 263001.
32  C. Barth, A. S. Foster, C. R. Henry and A. L. Shluger, *Adv. Mater.*, 2011, **23**, 477–501.
33  C. Barth and M. Reichling, *Nature*, 2001, **414**, 54–57.
34  J. V. Lauritsen, M. C. R. Jensen, K. Venkataramani, B. Hinnemann, S. Helveg, B. S. Clausen and F. Besenbacher, *Phys. Rev. Lett.*, 2009, **103**, 076103.
35  J. Wang, A. Howard, R. G. Egdell, J. B. Pethica and J. S. Foord, *Surf. Sci.*, 2002, **515**, 337–343.
36  S. Gritschneder, C. Becker, K. Wandelt and M. Reichling, *J. Am. Chem. Soc.*, 2007, **129**, 4925–4928.
37  S. Gritschneder, S. Degen, C. Becker, K. Wandelt and M. Reichling, *Phys. Rev. B: Condens. Matter*, 2007, **76**, 014123.
38  K. Venkataramani, S. Helveg, B. Hinnemann, M. Reichling, F. Besenbacher and J. V. Lauritsen, *Nanotechnology*, 2010, **21**, 265602.
39  M. C. R. Jensen, K. Venkataramani, S. Helveg, B. S. Clausen, M. Reichling, F. Besenbacher and J. V. Lauritsen, *J. Phys. Chem. C*, 2008, **112**, 16953–16960.
40  C. L. Pang, H. Raza, S. A. Haycock and G. Thornton, *Surf. Sci.*, 2000, **460**, L510–L514.
41  T. Becker, A. Birkner, G. Witte and C. Wöll, *Phys. Rev. B: Condens. Matter*, 2002, **65**, 115401.
42  M. A. Schildbach and A. V. Hamza, *Phys. Rev. B: Condens. Matter*, 1992, **45**, 6197–6206.
43  K. Simeonov and D. Lederman, *Surf. Sci.*, 2009, **603**, 232–236.
44  T. Hsu and Y. Kim, *Surf. Sci.*, 1991, **243**, L63–L66.
45  K. Markert, G. Beitel, J. Wiechers, J. Hrbek and R. J. Behm, *Adsorption on Ordered Surfaces of Ionic Solids and Thin films*, Springer, Berlin, 1993.
46  S. Curiotto and D. Chatain, *Surf. Sci.*, 2009, **603**, 2688–2697.
47  C. C. Chang, *J. Vac. Sci. Technol.*, 1971, **8**, 500–511.
48  J. G. Catalano, *J. Phys. Chem. C*, 2010, **114**, 6624–6630.
49  M. Bäumer and H.-J. Freund, *Prog. Surf. Sci.*, 1999, **61**, 127–198.
50  H.-J. Freund, *Surf. Sci.*, 2002, **500**, 271–299.
51  J. H. Kwak, J. Z. Hu, D. Mei, C. W. Yi, D. H. Kim, C. H. F. Peden, L. F. Allard and J. Szanyi, *Science*, 2009, **325**, 1670–1673.
52  S. A. Chambers, T. Droubay, D. R. Jennison and T. R. Mattsson, *Science*, 2002, **297**, 827–831.
53  J. H. Choi, D. Y. Kim, B. J. Hockey, S. M. Wiederhorn, C. A. Handwerker, J. E. Blendell, W. C. Carter and A. R. Roosen, *J. Am. Ceram. Soc.*, 1997, **80**, 62–68.
54  N. Ravishankar, V. B. Shenoy and C. B. Carter, *Adv. Mater.*, 2004, **16**, 76.
55  A. Ismach, L. Segev, E. Wachtel and E. Joselevich, *Angew. Chem., Int. Ed.*, 2004, **43**, 6140–6143.
56  C. T. Campbell, S. C. Parker and D. E. Starr, *Science*, 2002, **298**, 811–814.
57  S. C. Parker and C. T. Campbell, *Phys. Rev. B: Condens. Matter*, 2007, **75**, 035430.
58  S. Gritschneder, Y. Namai, Y. Iwasawa and M. Reichling, *Nanotechnology*, 2005, **16**, S41–S48.
59  S. Gritschneder and M. Reichling, *Nanotechnology*, 2007, **18**, 044025.
60  C. D. Wagner, W. M. Riggs, L. E. Davis, J. F. Moulder and G. E. Muilenberg, *Handbook of Photoelectron Spectroscopy*, Perkin-Elmer Corporation, Eden Prairie, 1979.
61  J. R. Heffelfinger and C. B. Carter, *Surf. Sci.*, 1997, **389**, 188–200.
62  J. R. Heffelfinger, M. W. Bench and C. B. Carter, *Surf. Sci.*, 1997, **370**, L168–L172.
63  S. Curiotto and D. Chatain, *Surf. Sci.*, 2009, **603**, 2688–2697.
64  H. C. Galloway, P. Sautet and M. Salmeron, *Phys. Rev. B: Condens. Matter*, 1996, **54**, 11145–11148.
65  M. Corso, W. Auwarter, M. Muntwiler, A. Tamai, T. Greber and J. Osterwalder, *Science*, 2004, **303**, 217–220.
66  G. Kresse, M. Schmid, E. Napetschnig, M. Shishkin, L. Kohler and P. Varga, *Science*, 2005, **308**, 1440–1442.
67  K. Pohl, M. C. Bartelt, J. de la Figuera, N. C. Bartelt, J. Hrbek and R. Q. Hwang, *Nature*, 1999, **397**, 238–241.
68  M. Bäumer and H. J. Freund, *Prog. Surf. Sci.*, 1999, **61**, 127–198.
69  N. Berdunov, G. Mariotto, K. Balakrishnan, S. Murphy and I. V. Shvets, *Surf. Sci.*, 2006, **600**, L287–L290.
70  C. Becker, A. Rosenhahn, A. Wiltner, K. von Bergmann, J. Schneider, P. Pervan, M. Milun, M. Kralj and K. Wandelt, *New J. Phys.*, 2002, **4**, 15.
71  S. Degen, C. Becker and K. Wandelt, *Faraday Discuss.*, 2004, **125**, 343–356.
72  M. Schmid, G. Kresse, A. Buchsbaum, E. Napetschnig, S. Gritschneder, M. Reichling and P. Varga, *Phys. Rev. Lett.*, 2007, **99**, 196104.
73  H. Brune, *Surf. Sci. Rep.*, 1998, **31**, 121–229.
74  P. Wynblatt and N. A. Gjostein, *Acta Metall.*, 1976, **24**, 1165–1174.
75  B. K. Chakraverty, *J. Phys. Chem. Solids*, 1967, **28**, 2401–2412.
76  F. S. Pettit, E. H. Randklev and E. J. Felten, *J. Am. Ceram. Soc.*, 1966, **49**, 199–203.
77  M. C. Wu, W. S. Oh and D. W. Goodman, *Surf. Sci.*, 1995, **330**, 61–66.